

Development of an experimental platform for the investigation of laser-plasma interaction in conditions relevant to shock ignition regime

Cite as: Rev. Sci. Instrum. **93**, 063505 (2022); <https://doi.org/10.1063/5.0089969>

Submitted: 02 March 2022 • Accepted: 25 May 2022 • Published Online: 23 June 2022

T. Tamagawa, Y. Hironaka,  K. Kawasaki, et al.



View Online



Export Citation



CrossMark

ARTICLES YOU MAY BE INTERESTED IN

[A multi-stage scintillation counter for GeV-scale multi-species ion spectroscopy in laser-driven particle acceleration experiments](#)

Review of Scientific Instruments **93**, 063502 (2022); <https://doi.org/10.1063/5.0078817>

[An angular-resolved scattered-light diagnostic for laser-plasma instability studies](#)

Review of Scientific Instruments **93**, 053505 (2022); <https://doi.org/10.1063/5.0090841>

[Hydroscaling indirect-drive implosions on the National Ignition Facility](#)

Physics of Plasmas **29**, 062705 (2022); <https://doi.org/10.1063/5.0080732>

Read Now!

Review of Scientific Instruments

Special Issue: Advances in Measurements and Instrumentation Leveraging Embedded Systems



Development of an experimental platform for the investigation of laser–plasma interaction in conditions relevant to shock ignition regime

Cite as: Rev. Sci. Instrum. 93, 063505 (2022); doi: 10.1063/5.0089969

Submitted: 2 March 2022 • Accepted: 25 May 2022 •

Published Online: 23 June 2022














View Online



Export Citation



CrossMark

T. Tamagawa,¹ Y. Hironaka,¹ K. Kawasaki,¹  D. Tanaka,¹ T. Idesaka,¹ N. Ozaki,²  R. Kodama,¹ R. Takizawa,¹ 
S. Fujioka,¹  A. Yogo,¹  D. Batani,³  Ph. Nicolai,³  G. Cristoforetti,⁴  P. Koester,⁴  L. A. Gizzi,⁴ 
and K. Shigemori^{1,a)} 

AFFILIATIONS

¹Institute of Laser Engineering, Osaka University, 2-6 Yamada-oka, Suita, Osaka 565-0871, Japan

²Graduate School of Engineering and Institute of Laser Engineering, Osaka University, 2-6 Yamada-oka, Suita, Osaka 565-0871, Japan

³Centre Lasers Intenses et Applications, CELIA, University Bordeaux CEA-CNRS, UMR 5107, F-33405 Talence, France

⁴Intense Laser Irradiation Laboratory, INO-CNR, 56124 Pisa, Italy

^{a)}Author to whom correspondence should be addressed: shige@ile.osaka-u.ac.jp

ABSTRACT

The shock ignition (SI) approach to inertial confinement fusion is a promising scheme for achieving energy production by nuclear fusion. SI relies on using a high intensity laser pulse ($\approx 10^{16}$ W/cm², with a duration of several hundred ps) at the end of the fuel compression stage. However, during laser–plasma interaction (LPI), several parametric instabilities, such as stimulated Raman scattering and two plasmon decay, nonlinearly generate hot electrons (HEs). The whole behavior of HE under SI conditions, including their generation, transport, and final absorption, is still unclear and needs further experimental investigation. This paper focuses on the development of an experimental platform for SI-related experiments, which simultaneously makes use of multiple diagnostics to characterize LPI and HE generation, transport, and energy deposition. Such diagnostics include optical spectrometers, streaked optical shadowgraph, an x-ray pinhole camera, a two-dimensional x-ray imager, a Cu K α line spectrometer, two hot-electron spectrometers, a hard x-ray (bremsstrahlung) detector, and a streaked optical pyrometer. Diagnostics successfully operated simultaneously in single-shot mode, revealing the features of HEs under SI-relevant conditions.

Published under an exclusive license by AIP Publishing. <https://doi.org/10.1063/5.0089969>

I. INTRODUCTION

The shock ignition (SI) scheme for inertial confinement fusion (ICF) relies on the use of pulsed lasers with different intensities (or a single tailored laser pulse) in the compression phase and the ignition phase.^{1–3} The scheme looks promising because it may reduce the impact of hydrodynamic instabilities, such as the Rayleigh–Taylor instability, since it allows using thicker (more massive) shells and low implosion velocities.^{4–6} In the SI scheme, the second (ignition) laser pulse needs to create a shock pressure of more than 300 Mbar at the ablation front, which is achieved

by using ($\approx 10^{16}$ W cm⁻²) high laser intensities.^{7,8} In this regime of laser–plasma interactions (LPIs), parametric instabilities, which grow nonlinearly, may become very strong and prevent the laser energy from being absorbed efficiently.^{9,10} Among LPIs, stimulate Raman scattering (SRS)¹¹ and two plasmon decay (TPD)¹² generate electron plasma waves, which in turn produce hot electrons (HE)² by damping. In the conventional approach to ICF, HEs are known to dramatically reduce the performance of target implosion due to fuel preheating.^{13,14} Instead, in SI, the high areal density achieved by the target at the beginning of the ignition phase can prevent HEs from penetrating deeply into the fuel and causing preheating. On

the contrary, under these conditions, the energy deposition from HEs could, indeed, increase the shock pressure and be beneficial for SI.¹⁵

Several experiments have already addressed the issue of LPIs and HEs in the SI laser intensity regime. Experiments at the National Ignition Facility (NIF)¹⁶ were performed to study LPI in direct-drive configuration with plasmas having density scale length of 500–700 μm and electron temperature of 3–5 keV.¹⁷

At the Shenguang-III¹⁸ laser facility in China, research on LPI has been performed by using 100 kJ of laser energy in indirect drive with a newly developed hohlraum design allowing to form mm-scale plasmas. The physics of LPI has been studied using more than 80 diagnostics and recording systems.¹⁹

Recent experiments were carried out at the LMJ-PETAL facility in France^{20,21} to characterize HEs generated by LPI in irradiated plastic layers and of studying their effect on the generation of a strong shock wave.²² The experiments confirmed that laser temporal smoothing can reduce LPIs and the density of high-energy HEs.

Experiments at the OMEGA-EP laser facility²³ have been focusing on characterizing the effect of HE population and energy distribution on target hydrodynamics and shock wave propagation. The simultaneous use of $K\alpha$ and bremsstrahlung diagnostics allowed to constrain the characterization of the HE source. The derived HE source was successively used as input in hydrodynamic simulations, accounting for HE transport and energy deposition as well, and the computed shock position was compared to the results obtained by time-resolved x-ray radiography.²⁴ The generated plasma had shorter scale lengths ($\sim 150 \mu\text{m}$) and lower temperatures ($\sim 2 \text{ keV}$) as compared to real SI conditions; however, under such conditions, it was shown that the generated HEs had a temperature low enough to produce a positive increase in shock velocity and pressure. Experiments performed at the Prague Asterix Laser Facility (PALS)^{25,26} allowed researchers to infer that part of laser energy was converted by SRS and SRS/TPD hybrid instabilities, generating a low flux ($\sim 0.1\%$) of low-energy ($\sim 20 \text{ keV}$) HE, possibly with a higher energy HE component ($\geq 100 \text{ keV}$). Again, the plasma scale length in this experiment was smaller than under real SI conditions.

Given this background, we have been developing an all-in-one experimental platform to study LPIs relevant to the SI conditions at the GEKKO-HIPER Nd:glass laser facility^{27,28} of the Institute of Laser Engineering (ILE), Osaka University. The GEKKO-HIPER facility has 12 laser beams that can irradiate planar targets. The total laser pulse energy is 4 kJ, which corresponds to an intensity exceeding $8 \times 10^{15} \text{ W/cm}^2$ in a 300 ps pulse and a 300 μm spot diameter at the fundamental laser frequency. The laser wavelength can be easily changed from the fundamental wavelength (1053 nm) to the second (527 nm) or the third harmonic (351 nm) by rotating the dihydrogen phosphate (KDP) crystals that are positioned just before the focusing lenses. This feature is particularly advantageous for the diagnosis of LPIs that strongly depend on the irradiation wavelength, and, indeed, experiments on the effect of laser conditions on LPIs and the transport of HEs have already been conducted.²⁹

This paper describes the latest developments of the experimental platform realized at the GEKKO XII-HIPER laser facility dedicated to investigate LPI and HE generation at laser intensities relevant to SI. The platform uses ten instruments of nine different types to characterize LPIs, the subsequent HE generation, and their transport and absorption. All diagnostics instruments acquire

data in a single laser pulse. LPI was characterized by diagnosing the spectrum of the light backscattered from the targets. In recent shots, the key observed parametric instabilities were convective SRS, which occurs in the convection region below a quarter of the critical density, as well as convective TPD and absolute SRS-TPD hybrid instability, which occur in the proximity of the quarter of the critical density. In addition, the plasma-density scale length, which characterizes the LPI threshold, could be estimated by comparing one-dimensional shadowgraphy images with hydrodynamic simulations. An x-ray pinhole camera served to determine the laser-spot diameter on the target. The energy of HEs and their spectrum was directly measured using two electron spectrometers (ESMs), and indirectly by recording the bremsstrahlung x-ray emission from the target. The transport of HEs in the target could be investigated by using a two-dimensional x-ray imager and an x-ray spectrometer collecting the Cu $K\alpha$ radiation emitted by a Cu tracer layer embedded into the target. The generated shock was finally characterized by using a streaked optical pyrometer (SOP) to record the optical emission from the target.

The remainder of the paper is organized as follows: Sec. II shows the laser configuration and the target conditions; Sec. III reports the details of the individual instruments on the platform and explains their role in measuring LPIs and hot electrons; Sec. IV presents the results from individual instruments acquired from a single laser pulse; and finally, Sec. V contains the conclusions.

II. EXPERIMENTAL BASELINE FOR DIAGNOSIS OF LASER-PLASMA INTERACTION AND HOT ELECTRONS

The experimental platform was developed on the HIPER irradiation system of the GEKKO XII facility,^{27,28} which allows on-side irradiation of flat targets with 12 beams. We present here the diagnostic capabilities and preliminary experimental results obtained at 2ω irradiation ($\lambda = 527 \text{ nm}$) and 3ω irradiation ($\lambda = 351 \text{ nm}$). Nine beams were converted at 3ω and combined into a 300 ps (Gaussian) pulse delivering 400–600 J energy on the target. The typical focal spot size was 300 μm at full width at half maximum (FWHM), providing an intensity of $1\text{--}2 \times 10^{15} \text{ W/cm}^2$. The three remaining beams operated at 2ω and were used as pre-pulses to produce a preformed longer scale length plasma. They delivered 200–300 J in 300 ps (Gaussian) and were focused to a typical focal spot size of 1000 μm FWHM for an intensity on the target of $1 \times 10^{14} \text{ W/cm}^2$. The 3ω and 2ω beams mounted random phase plates (RPP) and kinoform phase plates (KPP), respectively. The main 3ω pulse was delayed by 200 ps with respect to the 2ω pre-pulse.

Figure 1 shows a typical target configuration used in these preliminary shots. The target has three layers—polyethylene, Cu, and quartz. The polyethylene layer (10 μm thick) was placed on the laser-irradiated surface as an ablator. The Cu layer (25 μm thick) was sandwiched by polystyrene and quartz and served as a hot-electron marker by emitting $K\alpha$ photons as a result of HE absorption, which are successively detected by x-ray diagnostics. The 50- μm -thick quartz layer formed the rear surface and served to measure shock-wave temperatures via SOP. The shock-wave pressure is deduced from the shock-wave temperatures and the equation of state of the quartz.

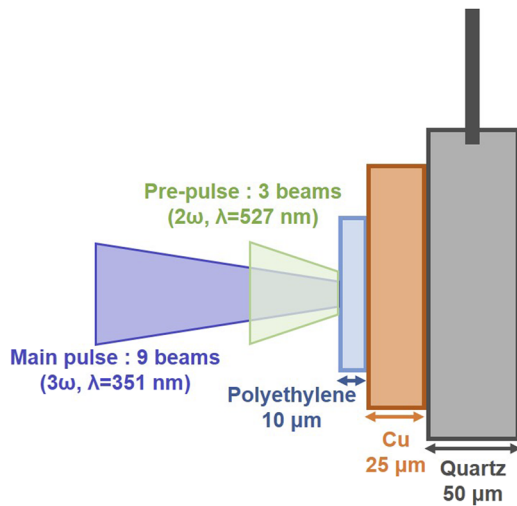


FIG. 1. Target and laser configuration. The main pulse and pre-pulse are the combination of nine and three individual beams, respectively. The target consists of three layers of the given materials and dimensions.

III. DESCRIPTION OF THE DIAGNOSTICS

Figure 2 shows the overall scheme of the experimental setup showing the position of each instrument, including its angle with respect to the target normal. Hereafter, we describe the ten diagnostics used in the platform.

A. Two different spectrometers for backscattered light generated by laser-plasma interactions

A time-resolved spectrometer and time-integrated spectrometer were employed to detect backscattered radiation originating from convective SRS at densities lower than $n_c/4$, as well as convective TPD and absolute SRS-TPD occurring near $n_c/4$, where n_c is the plasma critical density. Basically, the time-resolved spectrometer explores the time evolution of those instabilities, and the time-integrated spectrometer explores the overall backscattered spectrum

and its magnitudes, where the spectral position of the peaks allowed to determine the density regions where the different instabilities that are responsible for HE generation take place.

Part of the backscattered light generated by the target traveled backward along the path of the incident laser up to the turning mirror (which only reflected light at 1053 nm). It then passed through three different filters: a 400 nm high-pass filter, a 1000 nm low-pass filter, and a 527 nm notch filter. Finally, the backscattered light was focused by a Fresnel lens into a fiber and transported to the two spectrometers.

A 1.8 m quartz fiber transported the backscattered light to the time-integrated spectrometer (OCEAN optics, HR2000) with spectral resolution $\Delta\lambda \approx 2$ nm. For the time-resolved measurements, the backscattered light entered the spectrometer (Hamamatsu, A6365) through a 20 m quartz fiber. The dispersed spectrum with a wavelength between 500 and 800 nm, and spectral resolution of $\Delta\lambda \approx 3$ nm, was then detected by a streak camera (Hamamatsu, C7700) with a time window of 5.26 ns and a time resolution of 50 ps.

B. Plasma shadowgraph for density scale length measurement

The plasma length scale is important since it determines the threshold for the onset of parametric instabilities and, hence, HE generation. To estimate the plasma scale length, we used a side shadowgraph. During laser irradiation, a 1D shadowgraph of the plasma was obtained with a streak camera (Optronics, Optoscope SC-10) by sweeping a YAG laser beam converted to 2ω ($\lambda = 532$ nm) horizontally across the target. The transmitted light was filtered with a low-pass filter, a high-pass filter, and a 532 nm interferential filter. In the data shown in the following, the optical magnification was 30, the measurement time window was 2 ns, and the temporal and spatial resolutions were 10 ps and $10 \mu\text{m}$, respectively. As it is well known, the refraction effects in the plasma do not allow to perform measurements up to the plasma critical density for the probe laser beam (in this case, $n_c \approx 4 \times 10^{21}$ electrons/cm³) but only up to about 1/10 of the plasma critical density,^{30,31} depending on the plasma profile. Consequently, the region around $n_c/4$ for the 3ω laser beam could not be directly probed. Therefore, the plasma scale length and the density regions that are effectively probed could be

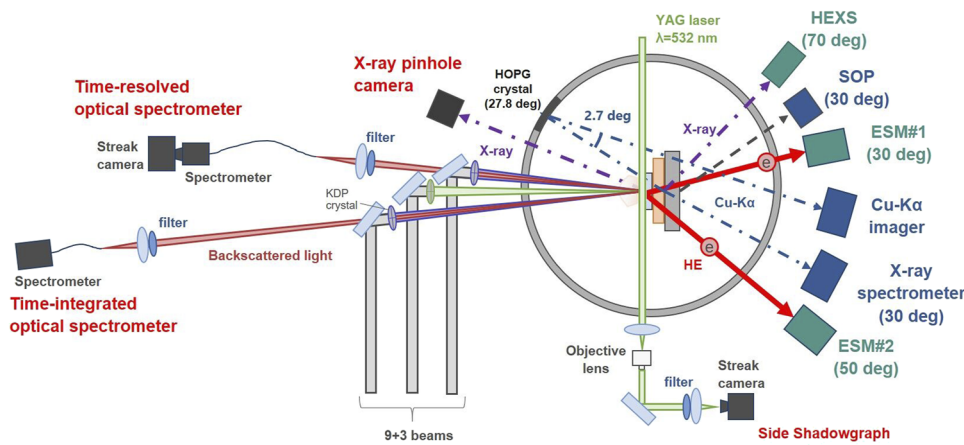


FIG. 2. Schematic top-view drawing of the experimental setup. The angle given below each instrument is the angle with respect to the target normal.

retrieved by comparing the experimental results with the results of the 1D plasma simulation.

C. X-ray pinhole camera to diagnose focal length and intensity of the main pulse

The focal length and the intensity of the laser pulse were determined by using the x-ray pinhole camera, which detected x rays generated by the laser-irradiated target. Two 25 μm -sized pinholes were used in the camera, with different filtering levels (no filter and 15 μm aluminum), allowing to record two images of the focal spot on a CCD camera to estimate its dimensions. The laser intensity on the target was calculated by using these images of the focal spot. In the results shown below, the pinhole camera magnification was 10 and the spatial resolution was 30 μm .

D. Electron spectrometer and high-energy x-ray spectrometer to determine energy of hot electrons

The energy of the hot electrons could be measured directly by an ESM³² and indirectly by a high-energy x-ray spectrometer (HEXS).³³ HEXS is also called “bremsstrahlung spectrometer”³⁴ or “a bremsstrahlung cannon”³⁵ in other facilities.

The ESM and the HEXS, as well as the x-ray spectrometer and Cu $K\alpha$ imager described in Sec. III E, used imaging plates (IPs) to record x rays and electrons (Fujifilm, FUJI Imaging Plate for research: BAS-MS).^{36,37} IPs accumulate time-integrated signals of radiation, such as x rays and electrons, and radiation recorded IPs were scanned using an IP scanner (GE Healthcare Japan, Typhoon FLA-7000) to obtain the information on the deposited energy. IP scanning was performed with the following parameters: resolution 25 μm , acceleration voltage 600 V, sensitivity 1.0, and latitude 5. The time between exposure and scanning was kept constant between 30 and 50 min.

In the ESM, a constant magnetic field (central magnetic field of 0.3 T) perpendicular to the direction of HE propagation curved their trajectory until they impacted on the IP located on the ESM wall. Electrons with higher kinetic energy follow a larger radius of curvature, allowing the energy dispersion of HE. Therefore, the intensity distribution recorded on the IP allows us to retrieve the energy distribution of electrons in a range from 60 keV to 1 MeV. The energy resolution depends on the resolution of the IP scanner and, here, increases nonlinearly from 0.1 keV (at 60 keV) to 0.8 keV (at 1 MeV), estimated by considering the Larmor motion of the electrons. Two ESMs were deployed at different angles from the target normal in order to discuss the angular dependence of the HE generation.

The HEXS collected x-ray fluence by using 12 IPs separated by interposed metal filters. Starting from the spectrometer entrance, the filters consisted of Al (100 μm), Ti (100 μm), Fe (100 μm), Cu (100 μm), Mo (100 μm), Ag (200 μm), Sn (500 μm), Ta (400 μm), Pb (1 mm), Pb (2 mm), Pb (3 mm), and Pb (4 mm). The signal recorded on the IPs allowed us to deduce hot electron spectra through the comparison with the experimental dose values and the counterpart from simulation calculations where hot electron spectrum was assumed. As a simulation procedure, first, x-ray spectra at the entrance of the HEXS resulted from the interaction of hot electrons with the target (CH and Cu layer) were calculated by using the PHITS code (Particle and Heavy Ion Transport Code System).³⁸

Second, x-ray spectra at the HEXS entrance were converted to dose value in each IP. In this process, a sensitivity curve calculated considering x-ray attenuation in each metal filter and IP themselves (PET, phosphor, and ferrite) was employed. Note that the calculation of the sensitivity curve of our used HEXS was performed using Monte Carlo simulations with GEANT4 in our collaborator work.³³ In this way, the HEXS also provides data for HE energies below 50 keV, a range that is inaccessible with the ESM.

E. X-ray spectrometer and imager for Cu $K\alpha$ emission

As explained in Sec. II A, the Cu layer of the target served as an HE tracer. By measuring the $K\alpha$ x rays generated from HE collisions with Cu atoms (followed by Cu inner shell ionization), we obtain the information on their penetration into the target and thus on their energy. The experimental platform includes two instruments for detecting the $K\alpha$ x-ray line—an x-ray spectrometer and a Cu $K\alpha$ imager. The results of both diagnostics can be used to deduce the number of HEs absorbed in the Cu layer of the target.

The x-ray spectrometer detects a spectrum within an energy band centered on the Cu $K\alpha$ line (8.048 keV). X rays entering the spectrometer are dispersed by a highly oriented planar graphite (HOPG) crystal and recorded on the IP in the spectral range from 7.4 to 8.4 keV, which includes the energy of the Cu $K\alpha$ line. The spectral resolution was $\Delta\lambda = 0.05$ keV.

The Cu $K\alpha$ imager produced a two-dimensional image of the Cu $K\alpha$ source.^{38,39} Generated x rays irradiated a bent HOPG crystal and only x rays near the Cu $K\alpha$ energy (8.048 keV) were reflected toward the IP placed on the opposite side of the target from the imager. The IP recorded the two-dimensional image of the Cu $K\alpha$ source. The result gives the size of the HE source and the intensity of Cu $K\alpha$ emission. X-ray images were recorded with a 17 \times magnification and digitized with a resolution of 1.5 μm .

F. Optical measurement to study the effect of hot electrons on the shock wave

In SI, HEs may enhance the shock pressure and preheat the plasma. In planar geometry experiments, the effect of HEs can be investigated by measuring the shock-wave parameters. A streaked optical pyrometer (SOP)⁴⁰ was used to determine the shocked target temperature. Here, in the SOP system, the self-emission from the shock front is recorded on a streak camera through an image relay system. In these shots, the optical magnification was 55, the measurement time range was 9.72 ns, and the temporal and spatial resolutions were 13 ps and 20 μm , respectively. The temperature is evaluated by using Planck’s law, which connects the optical emission to the temperature of a material. The temperature is then evaluated by using the following relation:

$$T = \frac{T_0}{\ln\left(1 + \frac{1-R}{I}A\right)}, \quad T_0 = \frac{hc}{\lambda_0}, \quad (1)$$

where h is Planck’s constant, c is the speed of light, λ_0 is emission wavelength, I is the optical intensity, R is the reflectivity of the shock front, and A is a unique constant that depends on the experimental setup. In our system, the optical emission is optically limited to 450 nm by bandpass filters. To determine A , we calibrated the SOP

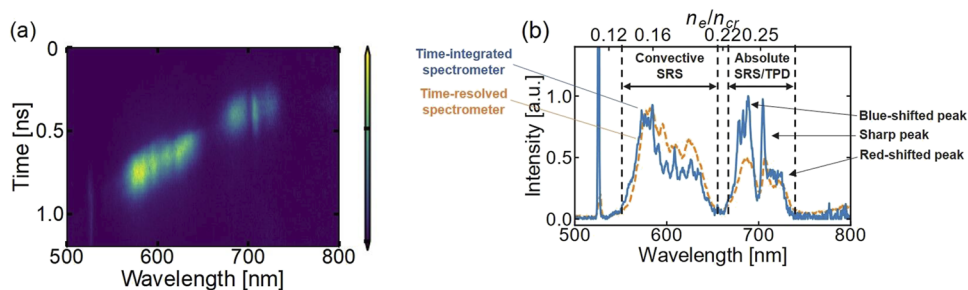


FIG. 3. (a) Backscatter spectrum from the time-resolved spectrometer before temporal and intensity calibration. The image shows a portion of 1 ns spectrum within the 5.26 ns time window. (b) Spectrum of time-integrated spectrometer (blue line) and vertical line profile of the spectrum in panel (a) (orange line).

by measuring the shock velocity with a VISAR system (velocity interferometer system for any reflector⁴¹), and we used the expressions of shock temperature and shock reflectivity as a function of shock velocity in quartz given in Ref. 42. In this way, we obtained $A = 890 \pm 290$ for our setup. Here, the target was rotated by 30° with respect to the laser beam in order to orient the normal to the target on the VISAR axis.

IV. EXPERIMENTAL RESULTS

In this section, we present the results obtained by each instrument for a single shot (SN44687). In this shot, the 3ω intensity of the main pulse was $2.2 \times 10^{15} \text{ W/cm}^2$ and that of the 2ω pre-pulse was $9.7 \times 10^{13} \text{ W/cm}^2$. The delay between the main pulse and the pre-pulse was 0.2 ns.

Figure 3(a) shows the result from the time-resolved spectrometer, and the black line in Fig. 3(b) shows the result from the time-integrated spectrometer. These results have been calibrated

temporally and spectrally. The signal acquired by the time-resolved spectrometer, in the spectral range from 500 to 800 nm, was corrected for the delay due to material dispersion incurred by passing through 20 m of quartz fiber. In both spectrometers, the signal intensity was calibrated by measuring the spectral sensitivity of each detector and fiber. The dashed line in Fig. 3(b) shows the integrated spectrum over time from the time-resolved spectrometer. This procedure enables to evaluate the validity of each diagnostic with each other. Since we observe the difference in spectrum intensity, we are going to introduce integrated spheres in order to remove chromatic aberration that would be the main source of the difference in the two diagnostics.

The relative intensities were rescaled by suitable factors for a fruitful comparison. The broad spectrum at wavelength below $\approx 660 \text{ nm}$ ($0.12 < n_e/n_c < 0.22$), which is the region within the green dashed lines in Fig. 3(b), is the signal produced by convective SRS. The spectrum in the region $660 \text{ nm} < \lambda < 740 \text{ nm}$, which is the area within the red dashed lines, is the signal originating from SRS

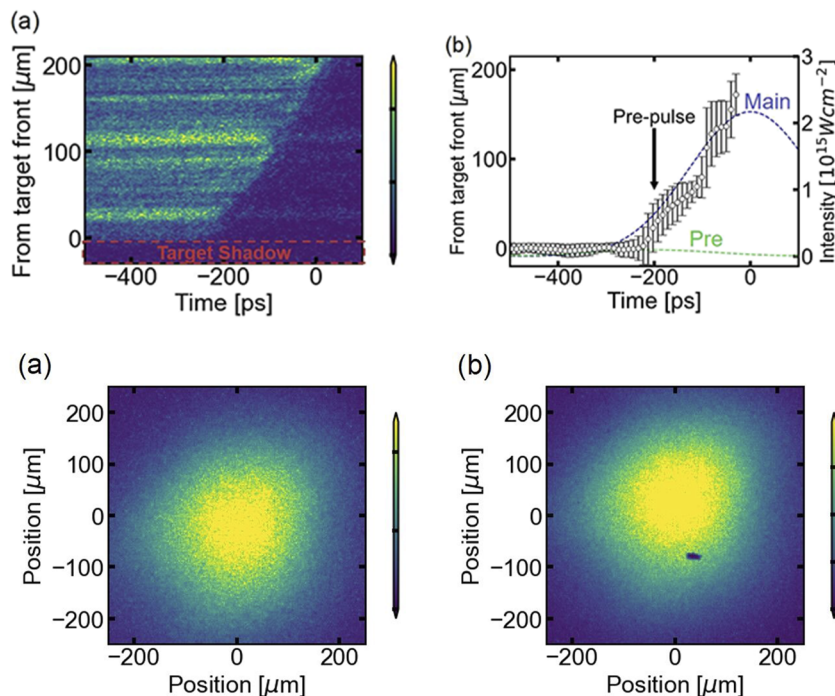


FIG. 4. (a) Raw image of side shadowgraph. (b) Boundary detection from the raw image: the variation over time of the position $\sim 1/10$ of critical density corresponding to the wavelength $\lambda = 532 \text{ nm}$. The circles show the position of the shadow region, and the black bars are the error bars. The blue and green dashed lines show waveforms of the main pulse and pre-pulse, respectively.

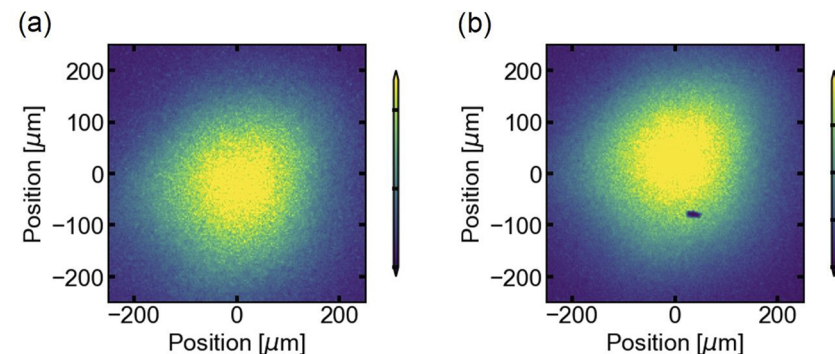


FIG. 5. Image produced by x-ray pinhole camera. (a) The result of filtering with a $15 \mu\text{m}$ aluminum filter. (b) The result of unfiltered image.

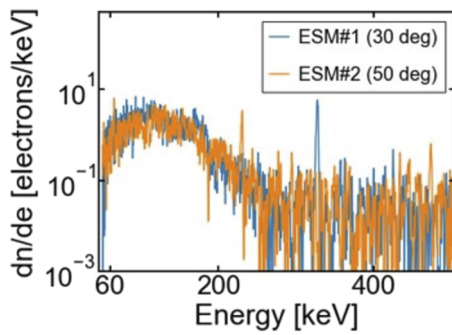


FIG. 6. Energy distribution of electrons measured by two ESMs. The blue line is the result of ESM No. 1 (30° from target normal), and the orange line gives the results of ESM No. 2 (50° from target normal).

and TPD instabilities driven in the proximity of the quarter critical density.^{26,43} Specifically, the sharp peak at $\lambda \sim 702$ nm is the signature of absolute SRS/TPD hybrid instability growing at $n_e \sim n_c/4$, while the broad peaks on its blue and red sides are produced by convective TPD driven at densities $0.21 < n_e/n_c < 0.24$.

For both results, the signal from convective and absolute SRS-TPD is confirmed, and both spectra are approximately consistent in shape. Note that the peak near 527 nm, attenuated by the notch filter, is assigned to the second harmonic and is produced when the laser pulse reaches the critical density.

We also performed calorimetry measurements of backscattered light. However, an accurate diagnosis was not possible because the intensity of the reflected 2ω pre-pulse became dominant, despite being filtered by notch filters. Since the calorimetry measurement of the backscattered light is important for quantifying the energy coupling during the LPI with respect to the incident laser energy, the next step is to make accurate calorimetry measurements from 500 to 800 nm.

Figure 4(a) shows the raw result of the side shadowgraph. The circles in Fig. 4(b) show the distance of the edge of the shadow from the target surface as a function of time. They were obtained from

lineouts of the shadowgraph at each time step, and the black bars are the error bars. The shadow corresponds to the region with a density of the order of 1/10 of the critical density for the YAG laser wavelength; the exact cutoff density can be estimated by ray-tracing analysis on the 2D maps of density obtained by hydrodynamic simulations. The vertical axis gives the distance from the target surface. The interval between the circles is the time resolution. The blue and green dashed curves show the waveforms of the main pulse and pre-pulse. The zero point of the horizontal axis is based on the laser timing of the main pulse; however, it includes an error of about 1 ns due to the timing jitter of the main pulse. These data are used to optimize the input parameters of the one-dimensional hydrodynamic simulation code ILESTA-1D.⁴⁴ The plasma length scale is estimated based on the results of the simulation with the optimized parameters as input.

Figure 5 shows a raw image of the x-ray pinhole camera. Figure 5(a) shows the result of filtering through a 15 μm aluminum filter, and Fig. 5(b) shows the result with no filter. Based on these results, the FWHM of the laser focal spot is estimated to be $2.8 \times 10^2 \mu\text{m}$ by Gaussian fitting. Although the CCD camera captures not only the main pulse (3ω) but also the pre-pulse (2ω) with a typical focal spot of 1000 μm , the estimated FWHM is dominated by the main pulse that is over 20 times more intense than the pre-pulse. Given this result, the intensity of the main pulse is estimated to be $2.5 \times 10^{15} \text{ W/cm}^2$.

Figure 6 shows hot electron spectra obtained from two ESMs. They are obtained from the raw IP data as follows: First, the electron kinetic energy corresponding to the position on the IP is calculated by considering the passage of electrons with energies ranging from 60 keV to 1 MeV through a constant magnetic field in the ESM. Next, the intensity detected by the IP is calibrated based on the energy sensitivity curve of the IP.^{45,46} Finally, the intensity is divided by the electron kinetic energy corresponding to the width of each pixel of the IP to obtain the number of electrons per unit energy (dn/de) as a function of the electron kinetic energy. The resulting energy distribution of electrons is shown in Fig. 6.

The results suggest that electrons with energy larger than 60 keV produce very similar signals in the two ESMs for this shot. The small number of HEs with energies around 60 keV is close to

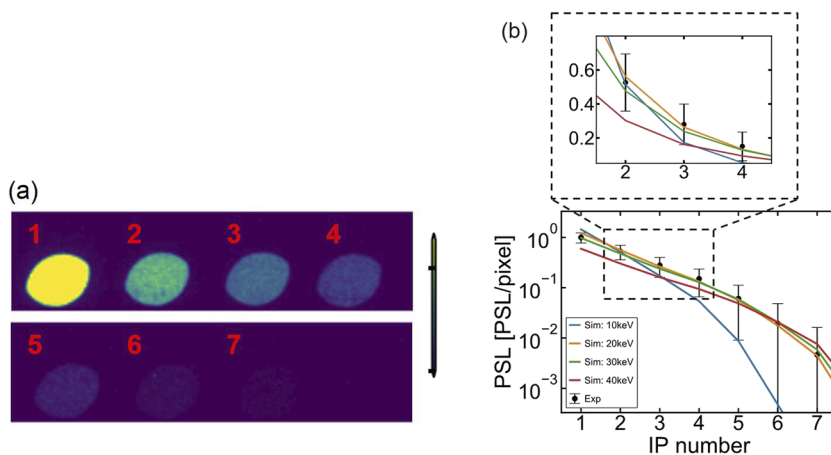


FIG. 7. (a) Raw image from seven IPs in the HEXS. The red number at the top-left of each image gives the IP number (the smaller the number, the closer to the entrance of the HEXS). (b) Experimental data from IPs in HEXS (black pints and bars) compared with the simulation results of PHITS. The colors indicate the input energy of hot electrons (blue = 10 keV, orange = 20 keV, green = 30 keV, red = 40 keV, Maxwellian distribution).

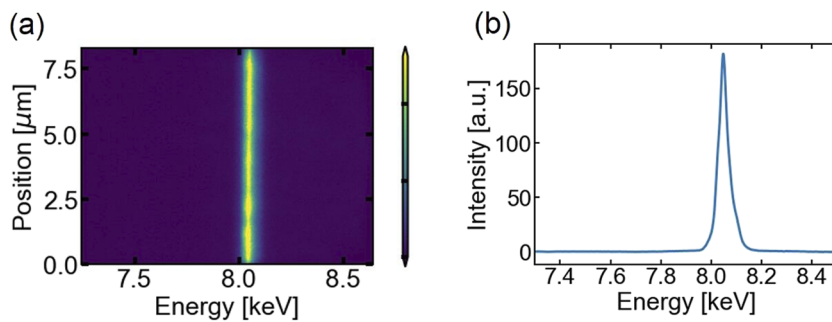


FIG. 8. Results of the x-ray spectrometer. (a) The raw image of IP and (b) the energy spectrum of Cu $K\alpha$ obtained by accumulating the raw data in the vertical direction.

the lower energy detection limit of the ESM. In both No. 1 and No. 2 results, exponential interpolations of energy between 100 and 300 keV with an exponential distribution [$dn/de = A \exp(E/T_{hot})$] yield an HE temperature (T_{hot}) between 20 and 30 keV. This is consistent with the results of the HEXS analysis described below.

Figure 7(a) shows the raw result of the HEXS, which gives another measurement of the energy of hot electrons. In the present experiment, the diagnosis was made with 12 IPs; however, for the analysis, we only used the first seven IPs, which had signals over five times greater than the background. To analyze the energy distribution of hot electrons from these data, we first simulated the passage of electrons through the target and the subsequent bremsstrahlung emission by using PHITS. The input was the energy distribution of the hot electrons, and we assumed a three-dimensional Maxwellian distribution with a single temperature (10, 20, 30, and 40 keV) in the initial stage of analysis. The simulation included the generation of bremsstrahlung emission through the interaction of the hot electrons with the target material until the bremsstrahlung x rays deposited their energy on the IPs in the HEXS. The output was the energy deposition by x rays on the seven IP layers. Next, we compared the experimental results of the HEXS with the output of the simulation converted to PSL values, which are unique values of the IP scanner [Fig. 7(b)]. Both experimental and simulation results were normalized by the PSL (photostimulated luminescence) value of the first IP. The horizontal axis gives the number of the IP (that of the smaller number was installed at the entrance of HEXS). The black bars give the standard deviation of the IP PSL value. The blue (10 keV), orange (20 keV), green (30 keV), and red (40 keV) lines correspond to the input HE temperature. Here, the single Maxwellian distribution was assumed in order to determine the dominant energy of hot electrons. The simulation

results for 20 or 30 keV are more consistent with the experimental results, and these results correspond with the temperature of exponential interpolation from the ESM result.

Figures 8(a) and 8(b) show the raw result and the line profile from the x-ray spectrometer, respectively. In the energy calibration of the horizontal axis of Fig. 8(b), the pixel including the peak signal corresponds to the energy of the Cu $K\alpha$ line (8.048 keV), and the energy width corresponding to a single pixel is calculated from the geometry of the spectrometer setup.

The raw result from the Cu $K\alpha$ imager is shown in Fig. 9(a). Figure 9(b) shows the line profile enclosed by the red dashed lines in Fig. 9(a) integrated vertically. The Gaussian fitting gives an FWHM of $1.9 \times 10^2 \mu\text{m}$, which is almost $100 \mu\text{m}$ smaller than the result of the x-ray pinhole camera, indicating that hot electrons are mainly generated in the more central part of the laser spot. Since the CH + Cu target thickness is only $35 \mu\text{m}$, the electrons do not possibly have much space to appreciably diverge from the origin to the Cu layer. Hence, we can conclude that $1.9 \times 10^2 \mu\text{m}$ is probably the real size of the HE sources. With a thicker target, this would not be the case: due to the angular expansion of HE, the source of $K\alpha$ is expected to be larger than the initial size of HE sources.

Figure 10 shows the raw streaked image from the SOP. The earliest sharp emission is due to emission from the preheating of hot electrons and/or high-energy x rays at the laser timing. The emission then fades when the shock wave transits into the Cu layer. Once the shock wave enters the transparent quartz layer, the self-emission from the shock front appears. From this simple analysis, the maximum temperature in the quartz layer is estimated to be 3 eV. More details on these data will be the subject of future publications.

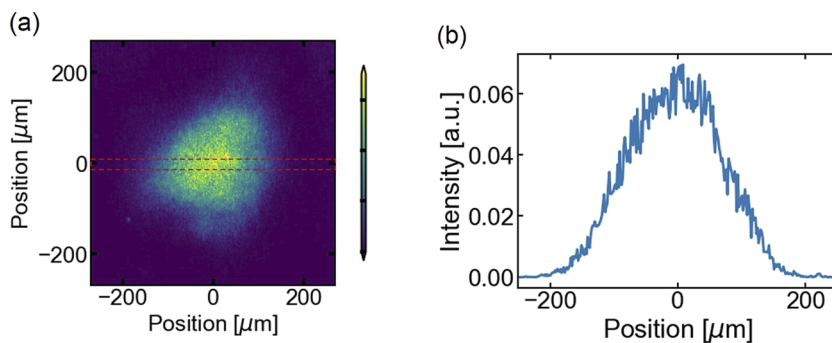


FIG. 9. Results of the Cu $K\alpha$ imager. (a) Raw image from the IP and (b) the vertical line profile of the region between the two red lines in (a). The vertical positioning of the red dashed lines was defined by applying a Gaussian fit to the vertical line profile of the raw data; the red lines were then positioned at the FWHM.

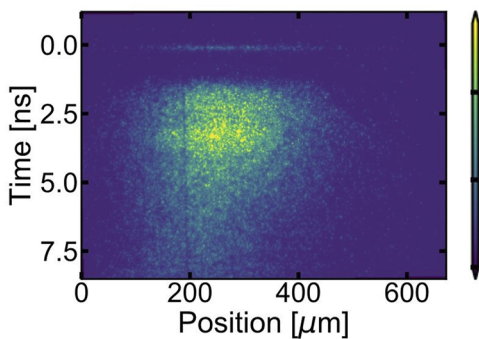


FIG. 10. Raw streaked image from SOP. The initial sharp emission is caused by preheating of hot electrons or high-energy x rays at the laser timing. Next, the emission fades as the shock wave passes through the Cu layer. When the shock wave enters the quartz layer, the self-emission from the shock front becomes visible.

V. CONCLUSION

We developed an experimental platform dedicated to perform research on hot-electron generation, transport, and energy deposition in a laser intensity regime of interest for the SI approach to inertial confinement fusion. The platform relies on the simultaneous use of ten different diagnostic instruments that can acquire data simultaneously in the same laser shot. Such a platform allowed obtaining experimental data under different target and laser conditions. In future work, we will upgrade the platform by including a backscattering calorimeter.

ACKNOWLEDGMENTS

The authors thank the staff at ILE for the dedicated technical support on laser operation, target fabrication, and plasma diagnostics. This work was done with the support and under the auspices of the NIFS Collaboration Research program (Grant No. 2021NIFS21KUGK136). This work was partly supported by the Japan Society for Promotion of Science, KAKENHI (Grant No. 17H02996), and grants from MEXT Quantum Leap Flagship Program (MEXT Q-LEAP) (Grant No. JPMXS0118067246).

AUTHOR DECLARATIONS

Conflict of Interest

The authors have no conflicts to disclose.

Author Contributions

T. Tamagawa: Conceptualization (equal); data curation (lead); formal analysis (lead); investigation (lead); methodology (equal); software (lead); validation (equal); visualization (equal); writing – original draft (lead); writing – review & editing (equal).
Y. Hironaka: Conceptualization (equal); data curation (equal); formal analysis (equal); investigation (equal); methodology (equal); resources (equal); supervision (equal); validation (equal); visualization (equal).
K. Kawasaki: Conceptualization (equal); data curation (equal); formal analysis (equal); investigation (equal); software (equal); validation (equal); visualization (equal); writing – original

draft (equal); writing – review & editing (equal).
D. Tanaka: Data curation (equal); formal analysis (equal); investigation (equal); methodology (equal); supervision (equal); validation (equal); visualization (equal).
T. Idesaka: Data curation (equal); formal analysis (equal); investigation (equal); methodology (equal); software (equal); validation (equal); visualization (equal); writing – original draft (equal); writing – review & editing (equal).
N. Ozaki: Data curation (equal); formal analysis (equal); investigation (equal); methodology (equal); supervision (equal); validation (equal); visualization (equal).
R. Kodama: Funding acquisition (equal); investigation (equal); project administration (equal); resources (equal); supervision (equal).
R. Takizawa: Data curation (equal); methodology (equal); supervision (equal); validation (equal).
S. Fujioka: Data curation (equal); formal analysis (equal); investigation (equal); methodology (equal).
A. Yogo: Data curation (equal); methodology (equal); supervision (equal); validation (equal).
D. Batani: Supervision (equal); validation (equal); visualization (equal); writing – original draft (equal).
Ph. Nicolai: Supervision (equal); validation (equal); visualization (equal); writing – original draft (equal).
G. Cristoforetti: Supervision (equal); validation (equal); visualization (equal); writing – original draft (equal).
P. Koester: Supervision (equal); validation (equal); visualization (equal); writing – original draft (equal).
L. A. Gizzi: Supervision (equal); validation (equal); visualization (equal); writing – original draft (equal).
K. Shigemori: Conceptualization (lead); data curation (equal); formal analysis (equal); funding acquisition (lead); investigation (equal); methodology (equal); project administration (lead); resources (lead); software (equal); supervision (lead); validation (lead); visualization (equal); writing – original draft (equal); writing – review & editing (lead).

DATA AVAILABILITY

All the experimental data have been saved in the SEDNA system at the Institute of Laser Engineering, Osaka University. The data that support the findings of this study are available from the corresponding author upon reasonable request.

REFERENCES

- R. Betti, C. D. Zhou, K. S. Anderson, L. J. Perkins, W. Theobald, and A. A. Solodov, *Phys. Rev. Lett.* **98**, 155001 (2007).
- L. J. Perkins, R. Betti, K. N. LaFortune, and W. H. Williams, *Phys. Rev. Lett.* **103**, 045004 (2009).
- D. Batani, S. Baton, A. Casner, S. Depierreux, M. Hohenberger, O. Klimo, M. Koenig, C. Labaune, X. Ribeyre, C. Rousseaux, G. Schurtz, W. Theobald, and V. Tikhonchuk, “Physical issues in shock ignition,” *Nucl. Fusion* **54**, 054009 (2014).
- G. I. Taylor, *Proc. R. Soc. London, Ser. A* **201**, 192 (1950).
- T. Ma *et al.*, *Phys. Rev. Lett.* **111**, 085004 (2013).
- J. Trela, W. Theobald, K. S. Anderson, D. Batani, R. Betti, A. Casner, J. A. Delettrez, J. A. Frenje, Y. Glebov, X. Ribeyre, A. A. Solodov, M. Stoeckl, and C. Stoeckl, *Phys. Plasmas* **25**, 052707 (2018).
- X. Ribeyre, M. Lafon, G. Schurtz, M. Olazabal-Loum e, J. Breil, S. Galera, and S. Weber, *Plasma Phys. Controlled Fusion* **51**, 124030 (2009).
- D. Batani, L. Antonelli, S. Atzeni, J. Badziak, F. Baffigi, T. Chodukowski, F. Consoli, G. Cristoforetti, R. de Angelis, R. Dudzak, G. Folpini, L. Giuffrida, L. A. Gizzi, Z. Kalinowska, P. Koester, E. Krousky, M. Krus, L. Labate, T. Levato, Y. Maheut, G. Malka, D. Margarone, A. Marocchino, J. Nejdli, Ph. Nicolai, T. O’Dell, T. Pisarczyk, O. Renner, Y. J. Rhee, X. Ribeyre, M. Richetta, M. Rosinski, M. Sawicka, A. Schiavi, J. Skala, M. Smid, Ch. Spindloe, J. Ullschmied, A. Velyhan,

- and T. Vinci, "Generation of high pressure shocks relevant to the shock-ignition intensity regime," *Phys. Plasmas* **21**, 032710 (2014).
- ⁹D. H. Froula *et al.*, *Plasma Phys. Controlled Fusion* **54**, 124016 (2012).
- ¹⁰A. Colaitis, G. Duchateau, X. Ribeyre, Y. Maheut, G. Boutoux, L. Antonelli, Ph. Nicolai, D. Batani, and V. Tikhonchuk, "Coupled hydrodynamic model for laser-plasma interaction and hot electron generation," *Phys. Rev. E* **92**, 041101(R) (2015).
- ¹¹D. W. Phillion, D. L. Banner, E. M. Campbell, R. E. Turner, and K. G. Estabrook, *Phys. Fluids* **25**, 1434 (1982).
- ¹²A. Simon, R. W. Short, E. A. Williams, and T. Dewandre, *Phys. Fluids* **26**, 3107 (1983).
- ¹³V. A. Smalyuk, D. Shvarts, R. Betti, J. A. Delettrez, D. H. Edgell, V. Yu. Glebov, V. N. Goncharov, R. L. McCrory, D. D. Meyerhofer, P. B. Radha, S. P. Regan, T. C. Sangster, W. Seka, S. Skupsky, C. Stoeckl, B. Yaakobi, J. A. Freije, C. K. Li, R. D. Petrasso, and F. H. Séguin, *Phys. Rev. Lett.* **100**, 185005 (2008).
- ¹⁴V. N. Goncharov *et al.*, *Phys. Plasmas* **15**, 056310 (2008).
- ¹⁵R. Nora, W. Theobald, R. Betti, F. J. Marshall, D. T. Michel, W. Seka, B. Yaakobi, M. Lafon, C. Stoeckl, J. Delettrez, A. A. Solodov, A. Casner, C. Reverdin, X. Ribeyre, A. Vallet, J. Peebles, F. N. Beg, and M. S. Wei, *Phys. Rev. Lett.* **114**, 045001 (2015).
- ¹⁶G. H. Miller, E. I. Moses, and C. R. Wuest, *Opt. Eng.* **43**, 2841 (2004).
- ¹⁷M. J. Rosenberg, A. A. Solodov, J. F. Myatt, W. Seka, P. Michel, M. Hohenberger, R. W. Short, R. Epstein, S. P. Regan, E. M. Campbell, T. Chapman, C. Goyon, J. E. Ralph, M. A. Barrios, J. D. Moody, and J. W. Bates, *Phys. Rev. Lett.* **120**, 055001 (2018).
- ¹⁸S. Jiang *et al.*, *Nucl. Fusion* **59**, 032006 (2019).
- ¹⁹F. Wang *et al.*, *Matter Radiat. Extremes* **5**, 035201 (2020).
- ²⁰N. Blanchot, G. Béhar, J. C. Chapuis, C. Chappuis, S. Chardavoine, J. F. Charrier, H. Coic, C. Damiens-Dupont, J. Duthu, P. Garcia *et al.*, *Opt. Express* **25**, 16957 (2017).
- ²¹M. Nicolaizeau and P. Vivini, *Proc. SPIE* **10084** (High Power Lasers for Fusion Research IV), 1008402 (2017).
- ²²S. D. Baton, A. Colaitis, C. Rousseaux, G. Boutoux, S. Brygoo, L. Jacquet, M. Koenig, D. Batani, A. Casner, E. Le Bel, D. Raffestin, A. Tentori, V. Tikhonchuk, J. Trela, C. Reverdin, L. Le-Deroff, W. Theobald, G. Cristoforetti, L. A. Gizzi, P. Koester, L. Labate, and K. Shigemori, *High Energy Density Phys.* **36**, 100796 (2020).
- ²³J. H. Kelly, L. J. Waxer, V. Bagnoud, I. A. Begishev, J. Bromage, B. E. Kruschwitz, T. J. Kessler, S. J. Loucks, D. N. Maywar, R. L. McCrory, D. D. Meyerhofer, S. F. B. Morse, J. B. Oliver, A. L. Rigatti, A. W. Schmid, C. Stoeckl, S. Dalton, L. Folsbee, M. J. Guardalben, R. Jungquist, J. Puth, M. J. Shoup III, D. Weiner, and J. D. Zuegel, *J. Phys. IV Fr.* **133**, 75 (2006).
- ²⁴A. Tentori, A. Colaitis, W. Theobald, A. Casner, D. Raffestin, A. Ruocco, J. Trela, E. Le Bel, K. Anderson, M. Wei, B. Henderson, J. Peebles, R. Scott, S. Baton, S. A. Pikuz, R. Betti, M. Khan, N. Woolsey, S. Zhang, and D. Batani, *Phys. Plasmas* **28**, 103302 (2021).
- ²⁵P. Koester *et al.*, *Plasma Phys. Controlled Fusion* **55**, 124045 (2013).
- ²⁶G. Cristoforetti, L. Antonelli, S. Atzeni, F. Baffigi, F. Barbato, D. Batani, G. Boutoux, A. Colaitis, J. Dostal, R. Dudzak, L. Juha, P. Koester, A. Marocchino, D. Mancelli, P. Nicolai, O. Renner, J. J. Santos, A. Schiavi, M. M. Skoric, M. Smid, P. Straka, and L. A. Gizzi, *Phys. Plasmas* **25**, 012702 (2018).
- ²⁷N. Miyanaga, M. Nakatsuka, H. Azechi, H. Shiraga, T. Kanabe, H. Asahara, H. Daido, H. Fujita, and K. Fujita, in *Proceedings of the 18th International Conference on Fusion Energy (IAEA), Sorrento, Italy, 2001* (International Atomic Energy Agency, 2001), p. IAEA-CN-77.
- ²⁸C. Yamanaka, Y. Kato, Y. Izawa, K. Yoshida, T. Yamanaka, T. Sasaki, M. Nakatsuka, T. Mochizuki, J. Kuroda, and S. Nakai, *IEEE J. Quantum Electron.* **17**, 1639 (1981).
- ²⁹K. Kawasaki, Y. Hironaka, Y. Maeda, T. Iwasaki, D. Tanaka, K. Miyaniishi, H. Nagatomo, S. Fujioka, N. Ozaki, R. Kodama, T. Matsuoka, D. Batani, J. Trela, P. Nicolai, and K. Shigemori, *High Energy Density Phys.* **37**, 100892 (2020).
- ³⁰D. Batani, J. Santos, P. Forestier-Colleoni, D. Mancelli, M. Ehret, J. Trela, A. Morace, K. Jakubowska, L. Antonelli, D. del Sorbo, M. Manclossi, and M. Veltcheva, "Optical time-resolved diagnostics of laser-produced plasmas," *J. Fusion Energy* **38**, 99 (2019).
- ³¹M. Tatarakis, R. Aliaga-Rossel, A. E. Dangor, and M. G. Haines, *Phys. Plasmas* **5**, 682 (1998).
- ³²T. Ozaki, S. Kojima, Y. Arikawa, H. Shiraga, H. Sakagami, S. Fujioka, and R. Kato, *Rev. Sci. Instrum.* **85**, 11E113 (2014).
- ³³S. Kojima *et al.*, *Commun. Phys.* **2**, 99 (2019).
- ³⁴C. D. Chen, J. A. King, M. H. Key, K. U. Akli, F. N. Beg, H. Chen, R. R. Freeman, A. Link, A. J. Mackinnon, A. G. MacPhee, P. K. Patel, M. Porkolab, R. B. Stephens, and L. D. Van Woerkom, *Rev. Sci. Instrum.* **79**, 10E305 (2008).
- ³⁵P. Koester, F. Baffigi, G. Cristoforetti, L. Labate, L. A. Gizzi, S. Baton, M. Koenig, A. Colaitis, D. Batani, A. Casner, D. Raffestin, A. Tentori, J. Trela, C. Rousseaux, G. Boutoux, S. Brygoo, L. Jacquet, C. Reverdin, E. Le Bel, L. Le-Deroff, W. Theobald, and K. Shigemori, *Rev. Sci. Instrum.* **92**, 013501 (2021).
- ³⁶T. Bonnet, M. Comet, D. Denis-Petit, F. Gobet, F. Hannachi, M. Tarisien, M. Versteegen, and M. M. Aleonard, *Rev. Sci. Instrum.* **84**, 013508 (2013).
- ³⁷G. Boutoux, D. Batani, F. Burgy, J. E. Ducret, P. Forestier-Colleoni, S. Hulin, N. Rabhi, A. Duval, L. Lecherbourg, C. Reverdin, K. Jakubowska, C. I. Szabo, S. Bastiani-Ceccotti, F. Consoli, A. Curcio, R. De Angelis, F. Ingenito, J. Baggio, and D. Raffestin, "Validation of modelled imaging plates sensitivity to 1-100 keV x-rays and spatial resolution characterisation for diagnostics for the 'PETawatt Aquitaine Laser,'" *Rev. Sci. Instrum.* **87**, 043108 (2016).
- ³⁸T. Sato, Y. Iwamoto, S. Hashimoto, T. Ogawa, T. Furuta, S. Abe, T. Kai, P.-E. Tsai, N. Matsuda, H. Iwase, N. Shigyo, L. Sihver, and K. Niita, *J. Nucl. Sci. Technol.* **55**, 684 (2018).
- ³⁹A. Morace and D. Batani, "Spherically bent crystal for X-ray imaging of laser produced plasmas," *Nucl. Instrum. Methods Phys. Res., Sect. A* **623**, 797-800 (2010).
- ⁴⁰P. M. Celliers, D. K. Bradley, G. W. Collins, D. G. Hicks, T. R. Boehly, and W. J. Armstrong, *Rev. Sci. Instrum.* **75**, 4916 (2004).
- ⁴¹D. G. Hicks, T. R. Boehly, J. H. Eggert, J. E. Miller, P. M. Celliers, and G. W. Collins, *Phys. Rev. Lett.* **97**, 025502 (2006).
- ⁴²P. M. Celliers, P. Loubeyre, J. H. Eggert, S. Brygoo, R. S. McWilliams, D. G. Hicks, T. R. Boehly, R. Jeanloz, and G. W. Collins, *Phys. Rev. Lett.* **104**, 184503 (2010).
- ⁴³G. Cristoforetti, A. Colaitis, L. Antonelli, S. Atzeni, F. Baffigi, D. Batani, F. Barbato, G. Boutoux, R. Dudzak, P. Koester, E. Krousky, L. Labate, Ph. Nicolai, O. Renner, M. Skoric, V. Tikhonchuk, and L. A. Gizzi, *Europhys. Lett.* **117**, 35001 (2017).
- ⁴⁴H. Takabe, M. Yamanaka, K. Mima, C. Yamanaka, H. Azechi, N. Miyanaga, M. Nakatsuka, T. Jitsuno, T. Norimatsu, and M. Takagi, *Phys. Fluids* **10**, 2884 (1988).
- ⁴⁵K. A. Tanaka, T. Yabuuchi, T. Sato, R. Kodama, Y. Kitagawa, T. Takahashi, T. Ikeda, Y. Honda, and S. Okuda, *Rev. Sci. Instrum.* **76**, 013507 (2005).
- ⁴⁶G. Boutoux, N. Rabhi, D. Batani, A. Binet, J.-E. Ducret, K. Jakubowska, J.-P. Nègre, C. Reverdin, and I. Thfoin, "Study of imaging plate detector sensitivity to 5-18 MeV electrons," *Rev. Sci. Instrum.* **86**, 113304 (2015).